Computational and Experimental Fluid-Structure Interaction Analysis of a High-Lift Wing with a Slat-Cove Filler for Noise Reduction

William D. Scholten, Ryan D. Patterson, Darren J. Hartl and Thomas W. Strganac
Department of Aerospace Engineering, Texas A&M University, College Station, TX 77843-3141

Quentin H. C. Chapelon
Mechanical Engineering Department, ÉNISE, Saint-Étienne, France

Travis Turner
Structural Acoustics Branch, NASA Langley Research Center, Hampton, VA 23681-2199

Airframe noise is a significant component of overall noise produced by transport aircraft during landing and approach (low speed maneuvers). A significant source for this noise is the cove of the leading-edge slat. The slat-cove filler (SCF) has been shown to be effective at mitigating slat noise. The objective of this work is to understand the fluid-structure interaction (FSI) behavior of a superelastic shape memory alloy (SMA) SCF in flow using both computational and physical models of a high-lift wing. Initial understanding of flow around the SCF and wing is obtained using computational fluid dynamics (CFD) analysis at various angles of attack. A framework compatible with an SMA constitutive model (implemented as a user material subroutine) is used to perform FSI analysis for multiple flow and configuration cases. A scaled physical model of the high-lift wing is constructed and tested in the Texas A&M 3 ft-by-4 ft wind tunnel. Initial validation of both CFD and FSI analysis is conducted by comparing lift, drag and pressure distributions with experimental results.

I. Introduction

Environmental noise from aircraft during the approach and landing phases of flight has become a major concern due to the increasing population growth around airports. Acoustic emissions from aircraft engines have been studied and reduced extensively such that now the airframe produces a comparable level of noise (known as airframe noise) during approach and landing. Significant contributions to airframe noise arise from wing high-lift devices: leading-edge slats, trailing-edge flaps. At high speeds, these devices stow against the main wing to reduce drag and improve cruise efficiency. During approach and landing (low speed flight), the high-lift devices are deployed to improve both the lift and stall characteristics of the aircraft, while also introducing geometric discontinuities to the airflow. These discontinuities, in turn, are the cause for considerable flow unsteadiness that generates airframe noise. For this work, the mitigation of the noise produced by the flow in the region of the slat is considered. One solution to mitigate the noise produced by the slat-cove is the slat-cove filler (SCF) [1], previously explored both computationally and experimentally [2–4]. The SCF reduces noise by filling the cove and guiding the flow along a specified path.

Previous work on the SMA-based SCF concept started with physical benchtop model development [5], which served as a basis for finite element models of the SCF. Optimization of the SCF design was conducted with an objective of minimizing the actuation force required for slat retraction. The optimization was subject to constraints on stress in the SMA components (primarily during retraction), deflection due to a static aerodynamic load (only while fully deployed) and SCF autonomous redeployment during deployment of the slat [6, 7]. Design optimization was also conducted for another SCF profile (the 30P30N airfoil [8]), followed by a study of various actuation load reduction methods [9]. Most recently, work was focused on the development of preliminary computational fluid dynamics (CFD) and fluid-structure interaction (FSI)

models on and comparing those results to early wind tunnel data [10].

This work is a continuation of the previous work [10] that sought to understand the behavior of the SMA SCF in flow using both computational tools and wind tunnel testing. Both the physical and computational models are based on a high-lift configuration of the Boeing-NASA Common Research Model (CRM[a]) [11] with an SMA SCF. Section II discusses the concept of the SMA SCF and the characteristics of the flow. Section III discusses the CRM geometry, the fluid model and CFD results for multiple CRM configurations. The FSI framework and results for a few load cases are discussed in Section IV. Section V discusses aspects of the physical wind tunnel model of the SCF and compares experimental and computational results. Finally, the work is summarized and future work is presented in Section VI.

II. Concept

Fig. 1(a) shows the typical landing condition flow field in the slat region. The flow bifurcates at the stagnation point on the slat. The lower portion of the flow then separates at the forward edge of the slat-cove resulting in a shear layer that reattaches near the trailing edge of the slat. The shear layer and its interaction with the recirculating flow in the slat-cove, the flow through the gap and the slat structure comprise many of the sources of airframe noise for the leading-edge slat.

The slat noise is reduced with the SCF by filling the cove and guiding flow along a specified path (see Fig. 1(b)). When deployed, the SCF must be stiff against aerodynamic loads to maintain its shape. It must also be compliant enough to retract into the slat-cove during stowage. In addition, the deformation the SCF undergoes during retraction to stow against the main wing exceeds what typical aerospace materials can achieve [5]. These conflicting requirements led NASA designers to incorporate superelastic shape memory alloys (SMAs) into the SCF design. SMAs are a type of active material that undergo a solid-phase transformation with temperature or stress, allowing for large recoverable inelastic deformation.

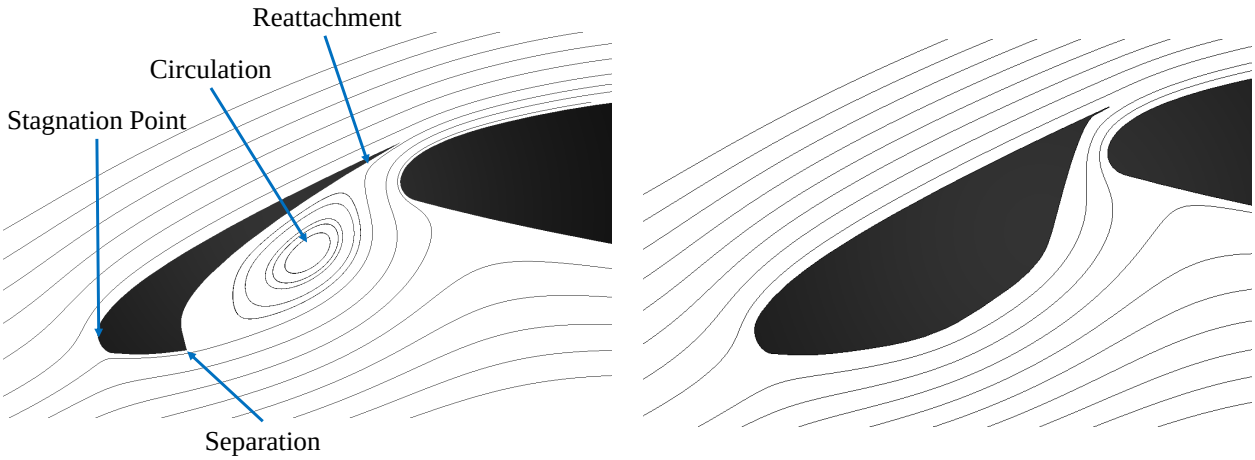

(a) Deployed. (b) Deployed with SCF.

Figure 1. Illustration of flow streamlines in vicinity of slat for a conventional airfoil.

III. CFD

Focus now shifts to the development and CFD analysis of fluid models for the SCF-treated airfoil. A general description of the model geometry is provided, from which the physical and computational models are based. Aspects of the physical model are also discussed, but a more detailed description of the physical model can be found in section V. Note that much of the computational work is done in congruence with experimental work.

[a]This particular geometry is an early version provided to the researchers before the final high-lift geometry of the CRM was available.

A. CRM Geometry

The SCF profile used in this work is for a high-lift variant of the Common Research Model (CRM), which is an open-source, transport-class aircraft geometry developed by Boeing and NASA primarily for new technology testing and validation of CFD analysis [11]. The baseline geometry for both the experimental and computational models in this work is a freestream-parallel section of the wing at the midspan of the outboard slat at 6.25% scale. At this scale, the chord of the reference section in its retracted configuration is approximately 0.32 m.

B. CFD Model

Prior to FSI analysis of the SCF, CFD models are constructed and tested, serving as a basis for FSI models. The thermo-fluid solver known as SC/Tetra [12] is used to conduct the CFD analysis. In this CFD suite, pressure and density finite volume methods are used to solve flow problems. SC/Tetra is considered for use in this work due to its unstructured meshing, built-in link to Abaqus for FSI analysis and the capability for overset meshes that allow for complex deformation such as slat/SCF articulation.

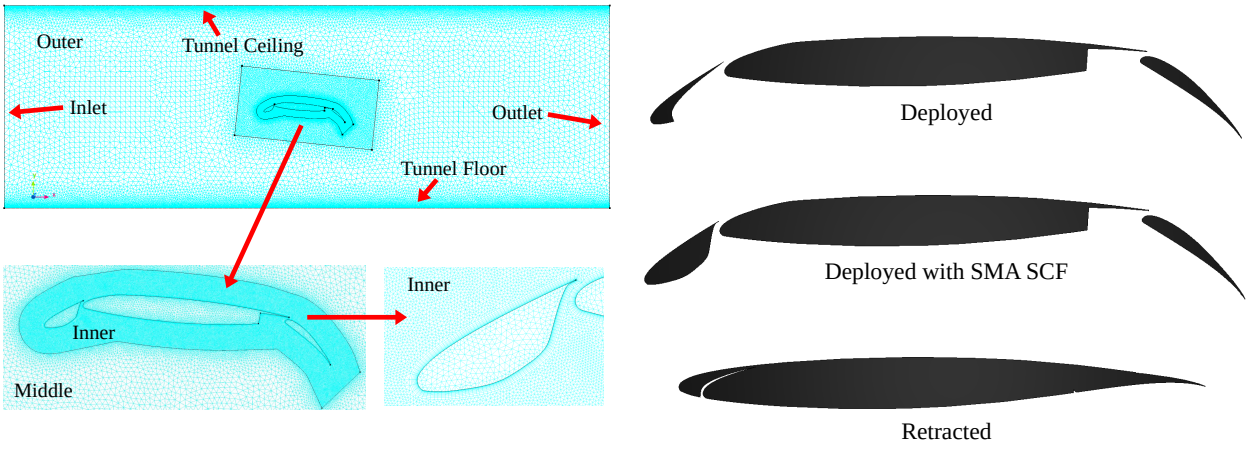

(a) CRM CFD model (mesh shown).

(b) Versions of CRM CFD models.

Figure 2. CFD model of CRM airfoil.

Both the wind tunnel test section and scaled wing are modeled in SC/Tetra (see Fig. 2(a)). Also, there are versions of the CFD model for each configuration of interest (see Fig. 2(b)): 1) deployed without the SCF, 2) deployed with the SCF and 3) retracted. The overall fluid model is based on the Texas A&M University 3 ft-by-4 ft tunnel (test section length is 2.74 m) used in testing the physical model. Also, the fluid model is 2D (one element in spanwise, Z, direction) with z-symmetry boundary conditions to model the spanwise uniform physical model that spans the tunnel width. The spanwise length of the CFD model is 1.27 cm. Other orientations are considered by rotating the closed volumes of the wing, inner fluid region and middle fluid region about the physical model's rotation point (x=-44.45 mm, y=0 mm). The original orientation of the provided geometry is at an angle of attack (AoA) of -1.48°. The midchord of the retracted configuration at this angle is taken as the origin for the CFD model.

The overall fluid model is composed of three closed volumes (excluding the solid parts): 1) inner, 2) middle, and 3) outer. The shape of the inner region is specified by a 10% retracted-chord offset from the solid wing. A box centered about the midchord of the retracted wing with dimensions of 1-chord by 2-chords defines the middle region. The remaining volume of the fluid domain is the outer region. Element sizes are specified for each region in the model in order to reduce computational runtime while maintaining accuracy in the various fluid regions, particularly in the inner region near the wing. The surfaces in the outer region corresponding to the tunnel floor and ceiling have the same refinement as the inner region to adequately capture the effects from the tunnel walls. The element size in each region is based on mesh studies that evaluated changes in lift and drag of the wing due to changes in the element size of each region. To better capture the boundary layer, prism layers are inserted along the surface of the wing and tunnel floor and ceiling. Parameters for the prism layers are based on results of a prism layer study conducted

with the deployed-with-SCF configuration. Both deployed configurations have approximately 200,000 elements (130,000 Prism and 70,000 Hexahedron) while the retracted configuration has approximately 187,000 elements (119,000 Prism and 68,000 Hexahedron).

The CFD model has three boundary conditions applied to it: 1) smooth, no-slip walls on the surface of the wing and the floor and ceiling of the tunnel, 2) zero static pressure at the outlet, and 3) freestream conditions (velocity and turbulence properties) at the inlet. The fluid considered in all analyses is incompressible air with a density of 1.206 kg/m^3 and a viscosity of 1.83x10^{-5} Pa-s. For most of this work, an inlet speed of 15 m/s (approximately Mach 0.044) is considered. Turbulence is modeled using the Shear-Stress Transport (SST) k-ω turbulence model [13], which is a low Reynolds number turbulence model that incorporates a zonal treatment between near-boundary flow and flow away from the boundaries. This model requires the specification of the turbulent energy k and the turbulent dissipation rate ε at the inlet, where ε is proportional to k and the dissipation rate per unit turbulence energy ω. These values are currently unknown so two flow cases are considered: 1) approximately laminar inlet flow and 2) fully developed turbulent inlet flow. For approximately laminar flow, k and ε are specified as default values (k=0.0001 m^2/s^2, ε=0.0001 m^2/s^3). For fully developed turbulent flow at the inlet, the following equations are used to calculate k and ε

$$k = \frac{u^2}{100}, \quad \varepsilon = \frac{0.09^{\frac{3}{4}} \cdot k^{\frac{3}{2}}}{0.07D} \tag{1}$$

where D is the equivalent diameter (currently the height of the test section 0.91 m). At an inlet speed of 15 m/s, the values of ε and k are 8.66 m^2/s^3 and 2.25 m^2/s^2, respectively.

C. CFD Results

Results from CFD analysis serve as a baseline for comparisons with experimental data, FSI analysis and other fluid codes. CFD analysis is conducted for the three airfoil configurations between angles of attack (AoA) of -2° and 12° and at an inlet speed of 15 m/s. Each CFD simulation is run until the solution (particularly the lift and drag) converges to a steady value (approximate fluctuation of 0.01 in the lift coefficient). Flow results between 4° and 8° are of particular interest since that is the typical AoA range for approach and landing.

The lift (C_l) and drag (C_d) coefficients for each configuration are obtained by extracting the viscous and pressure forces acting on the wing and normalizing them by span of the model, freestream dynamic pressure and chord of the retracted configuration. The lift-AoA curves of the retracted and deployed configurations for both inlet flow cases (≈laminar and fully developed turbulent) are shown in Fig. 3.

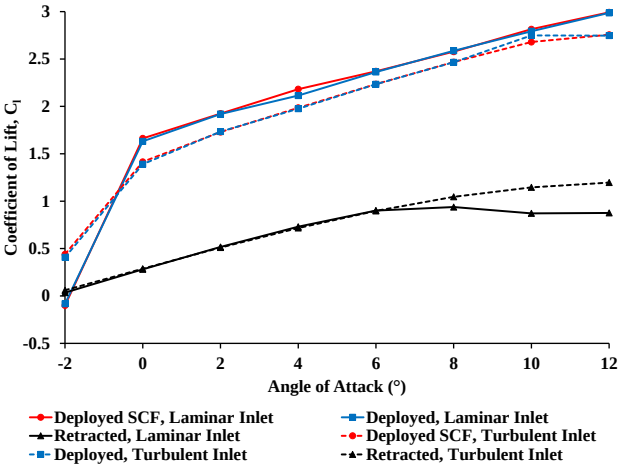

Figure 3. Comparison of CRM lift-AoA curves.

As shown in the figure, the zero-lift angle of attack for the retracted configuration is slightly lower than -2°, and the curve is approximately linear between -2° and 6°. In addition, the lift of the retracted configuration is approximately the same value in this AoA range for both inlet cases. Under ≈laminar inlet flow, the lift-AoA curve for the retracted configuration begins to flatten at AoA above 6°(i.e., the lift-curve slope is constant to 6°angle of attack), indicating that the configuration is approaching its maximum lift. Lift decreases with further increases in the angle of attack above 8°, indicating that the retracted configuration is stalling. However, for fully developed turbulent flow, the lift-AoA curve approximately is linear to 8°. The curve begins to flatten at higher angles, signaling that the configuration is near maximum lift, but it does not reach stall at the highest angle of attack considered.

Both deployed configurations exhibit an increase in lift compared to the retracted configuration, as expected. Also, both deployed configurations (for the same inlet case) have similar values of lift coefficient, indicating that the addition of the SCF is not negatively impacting the lift of the wing. In general, under ≈laminar inlet flow, the deployed configurations have higher lift compared to when the configurations are

under fully developed turbulent flow, also as expected. For both inlet flows, the lift-AoA curve is approximately linear between 0° and 10°(i.e., the lift-curve slope is constant to 10°angle of attack). Past 10°, the curves for the two flow cases begin to diverge. For ≈laminar inlet flow, the lift-AoA curve maintains its linear trend while for fully developed turbulent inlet flow, the curve begins to flatten, indicating that the maximum lift for both configurations is being approached. Below an angle of attack of 0°, the lift decreases significantly for all deployed cases due to significant separation of the flow across the lower surface of the main wing.

IV. FSI

Focus now shifts to FSI analysis of the SCF. A brief discussion of the structural model is given as well as changes to the fluid model and how the fluid and structural models are connected. Two cases are discussed in this work: 1) aerodynamic loading of the SCF in the fixed, fully deployed configuration and 2) retraction of the slat in flow.

A. Structural Model

Figure 4(a) shows the structural finite element model for FSI analysis of the SMA SCF. All components of the model are 10.27 mm (0.5 in) in spanwise (Z) length. The hinge, main wing and slat are rigid bodies while the SCF is the only deformable part. The hinge is fairly simple. For this work, both the hinge length and position are fixed, based on design choices made during the physical model development. The hinge axis is against the cove wall and the hinge length is 8 mm. Due to fabrication constraints such as SMA thickness and connecting the parts together, only monolithic SMA SCF designs are considered. For this work, the thickness of the SCF is set to 0.0762 mm (0.003 in) (same as the physical model). The SCF is meshed with 265 general shell elements (type S4) [14] along its curve and one element in the spanwise direction. Symmetry conditions are applied to the edges of the SCF in their respective X-Y planes, essentially making the span infinitely long ("2.5-dimensional"), which allowed for the implementation of one element in the spanwise direction.

In the normal direction, contact is modeled using surface-to-surface contact with a linear penetration penalty law in Abaqus while in the tangential direction, contact is modeled using a coefficient of friction of 0.42[b].

This model has two load cases that can be analyzed outside of FSI analysis. The first load case is a static aerodynamic loading for the fully deployed configuration using pressure data from CFD analysis. The second load case is retraction and deployment of the SCF.

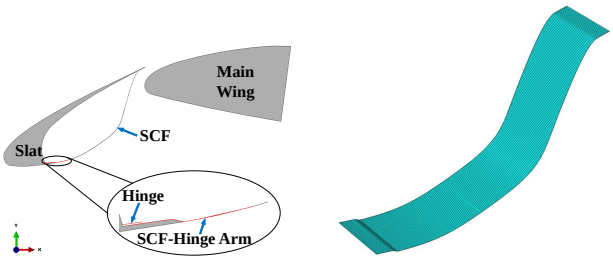

(a) Assembly. (b) SMA SCF mesh.

Figure 4. SMA SCF structural model.

Table 1. SMA material properties.

Property	Value
(Elastic Properties)	
E_A,E_M	44.2 GPa, 26.4 GPa
$\nu_A = \nu_M$	0.33
(Phase Diagram Properties)	
M_s, M_f	236.9 K, 236.5 K
A_s, A_f	266.6 K, 268.1 K
$C^A = C^M$	7.1 MPa/K, 7.7 MPa/K
(Transformation Strain Properties)	
$H = H_v$	5.15%
(Smooth Hardening Properties)	
n_1, n_2, n_3, n_4	0.5
(Other Properties)	
ρ	6480 kg/m^3
$\alpha_M = \alpha_A$	0

[b]This value corresponds to the coefficient of friction for 3D printer plastic and SMA material (determined experimentally).

Capturing the thermomechanical behavior of SMA materials requires specialized constitutive models. For this work, the constitutive model developed by Lagoudas and coworkers [15] is used, and is implemented in Abaqus as a custom material (UMAT). The material properties for the UMAT are shown in Table 1. These properties are calibrated using tension tests of dogbone specimens (per ASTM standard [16]) made out of the same material used in the physical SCF. As seen in Fig. 5, the hysteresis loops from the calibrated UMAT and tension tests match well.

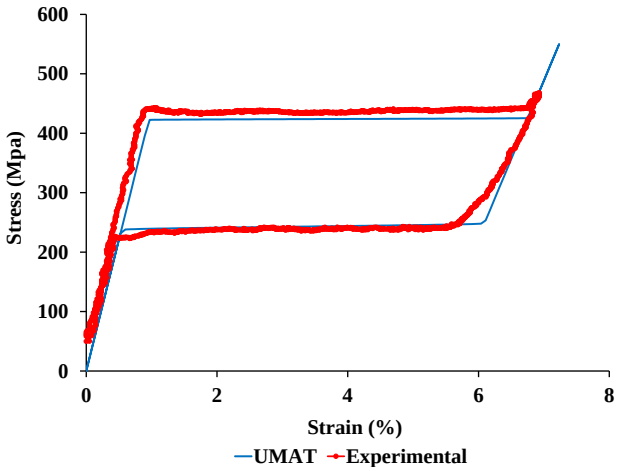

Figure 5. Hystersis loops of experimental data and calibrated UMAT.

B. Changes to Fluid

To be compatible with FSI analysis, the fluid model requires some changes. During retraction of the slat, the SCF is stowed into the small space between the leading edge of the main wing and the cove wall of the slat, resulting in significant volume reduction and elimination. The elimination of volume leads to fluid elements with zero volume, which introduces numerical instabilities to the analysis. Remeshing of the fluid model can be performed to handle the changing fluid volume. However, remeshing is computationally expensive. Another approach to the change in volume is the implementation of an overset mesh, which allows movable, deformable slave meshes to coincide with a master mesh. Compared to remeshing, an overset mesh implementation requires significantly less computational runtime. Flow data is transferred using interpolation between the surface of the slave mesh and the elements of the master mesh surrounding the slave mesh. Better interpolation can be achieved by using a master mesh that is more refined than the slave mesh. Note that the master region is assigned to areas during computations where multiple slave meshes overlap, which can lead to some boundary conditions (such as walls) being canceled. This potential loss of boundary conditions influences the design of both the slave and master meshes.

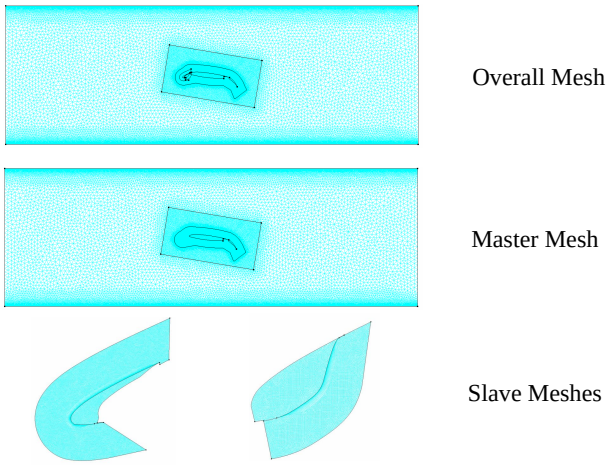

Figure 6. Overset mesh implementation.

The implementation of the overset mesh can be seen in Fig. 6. For this work, the flap, main wing and test section of the tunnel are part of the master mesh since those regions are fixed during the FSI analyses that is conducted. In the overset implementation, the SMA SCF and slat are slave meshes in order to perform retraction/deployment during the analysis. To help accommodate the large volume change, the slat and SCF are separated into two slave meshes.

With the implementation of the overset mesh and separation of the slat and SCF, new boundary conditions are needed for the slat-cove. Specifically, a zero static pressure boundary condition is applied to the fluid in the slat-cove in order for the enclosed, incompressible fluid volume to deform. Without the boundary condition, numerical instabilities are created by any SCF deformation that cause the analysis to become unstable. In addition, the interior of the slat is assigned as a fluid with the same zero static pressure boundary condition since early FSI attempts showed this to be beneficial to the convergence of the analysis.

Initial FSI attempts of slat retraction showed that when the SCF contacted the main wing, numerical instabilities were created and led to the crash of the analysis. This instability is avoided in the current work by negatively offsetting the main wings outer mold line in the fluid model by 0.127 mm. Therefore, when the SCF and main wing come into contact in the structural model due to slat retraction, a small gap separates

the two parts in the fluid model, preventing the creation of the instabilities due to contact.

The final significant change to the fluid model is the adjustment of the element sizes. The mesh of the master is refined such that the mesh in the slave regions is similar to the one in the CFD analysis. The prism layer parameters are also adjusted such that the total thickness of the prism layer is the same as the CFD model without causing mesh distortion. Note that prism layers are not inserted in areas where both slave meshes initially overlap to avoid numerical errors that results from the canceling of a boundary condition.

C. Linking Solvers

SC/Tetra is linked to Abaqus using a built-in connection with the Abaqus Co-simulation Engine, making FSI analysis easier to conduct. A weakly coupled scheme is used meaning that Abaqus and SC/Tetra solve their physical quantities and exchange information at specified time steps. Abaqus provides displacement of a specified surface to SC/Tetra while SC/Tetra provides pressures acting on that surface. Time is incremented using the time marching technique known as Gauss-Seidel. With this technique, the (n+1)th cycle of the structural model is calculated in Abaqus using data from the nth cycle of the fluid model in SC/Tetra. Then the displacement data of the (n+1)th cycle for the structural model is used to calculate the (n+1)th cycle of the fluid model. For this work, the FSI analysis is informed by an initial CFD analysis of the fluid model that is conducted until the flow becomes quasi-steady at a chosen cycle (cycle n). Specifically, the input data from the CFD analysis is set as the data for the nth cycle in the FSI analysis and is used by Abaqus to calculate the (n+1)th cycle of the structural model. The computational runtime is significantly reduced using initial CFD data since the flow does not have to develop in FSI analysis. Both solvers have a time step of 0.00005 s. The fluid model records data every 0.005 s while the structural model records results every 0.0005 s. Note that the pressure and viscous forces on the surface of the wing are recorded every cycle.

This framework requires that structural and fluid models have the same coordinate system. Thus, unique computational models are created for every angle of attack considered. The SMA SCF is the only deformable part so the solvers are only linked through its surface.

D. FSI Results: Fixed Fully Deployed

Aerodynamic loading of the SCF in the fully deployed configuration is the first FSI analysis considered. The hinge can freely rotate while the slat is fixed. This analysis is conducted on models at 6° and 8° AoA for inlet flow at 15 m/s using results from an initial CFD analysis as input data. The SCF displacement over time for both angles, corresponding to the maximum deflection point, is shown in Fig. 7(a). The displacement fluctuates at the start of FSI analysis, but dampens to a much smaller value by 0.1 s. The average maximum displacement for 6° and 8° are 0.0298 mm and 0.0290 mm (approximately 40% of the SMA thickness), respectively, which are reasonable when compared to the displacement from static analysis. As shown in Fig. 7(b), the SCF displacement from FSI analysis is similar to the displacement from static analysis. Differences in the pressure distribution between FSI and static analysis due to the implementation of the overset mesh and the fluctuation of the SCF account for differences in the displacements. Fourier analysis of the displacement for the last 0.25 s (512 data points) of FSI analysis shows that the SCF appears to be vibrating at a fundamental frequency of 74 Hz and 50 Hz for 6° and 8° AoA, respectively, and at harmonics of those fundamental frequencies. However, the root-mean-square of the dynamic response is quite small. Additionally, the initial CFD analysis has very small fluctuations in lift that have similar frequencies so additional work is needed to determine if the SCF vibration is physical or if it is a result of numerical noise.

E. FSI Results: Retraction

The other FSI analysis case considered is retraction and deployment of the slat in flow. Currently, only slat retraction is conducted. Note that retraction of the slat under flow at landing conditions is not physically meaningful. However, slat retraction under flow deforms the SCF mesh into a suitable configuration for deployment while maintaining the walls for the slat and SCF. At the time of this work, FSI retraction is conducted using a previous iteration of the fluid model. The previous iteration of the fluid model has approximately 1,360,000 elements and is created using similar modeling techniques (overset mesh, offset of main wing) as the current iteration. In addition, SMA properties from previous work [7] are used. The hinge

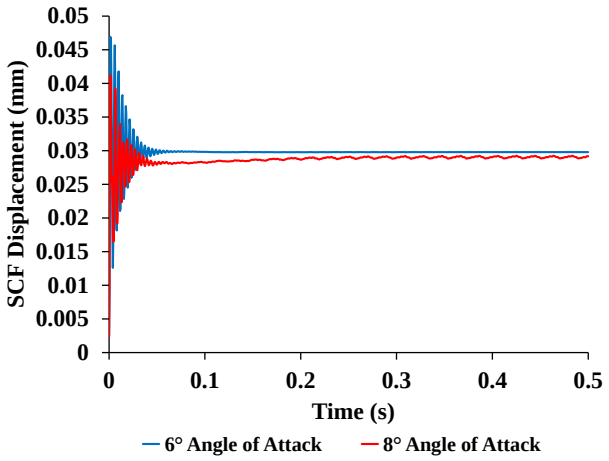

(a) SCF displacement overtime in FSI analysis .

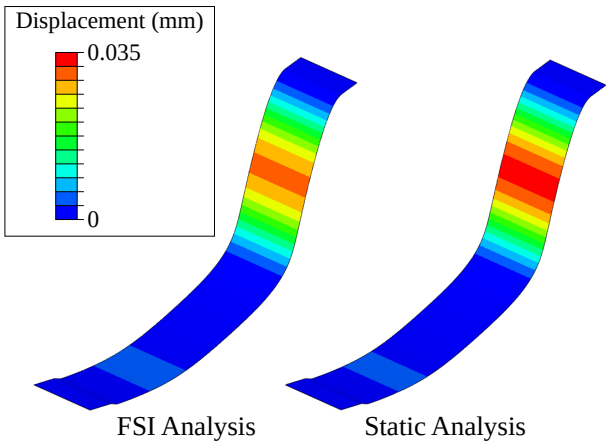

(b) Comparison of SCF displacement.

Figure 7. FSI results for fixed, fully deployed configuration.

length is 1.5 mm and the axis is placed 0.5 mm away from the cove wall.[c] In both the structural and fluid models, the slat is retracted over 2 s about its reference point (in the structural model). This retraction is faster than actual slat retraction, but it is needed to avoid significant computational runtimes. As with the fixed, fully deployed analysis case, data from CFD analysis of the fluid model is used to initialize the FSI retraction analysis. This analysis requires multiple days to run, but crashes at 94% retraction because of a zero volume fluid element related to the SCF. The zero volume element is due to mesh deformation associated with hinge rotation, deformation of the SCF and slat rotation. Figure 8 shows the velocity contours in the vicinity of the SCF at different stages of retraction. Any velocity inside the slat-cove is due to slave meshes overlapping each other and cannot be prevented. Also, the interpolation between the slave and master meshes creates local disturbances in the flow, which are present at all levels of retraction. The outer surfaces of the slave meshes (and thus the disturbances) are away from the surface of the wing and the influence of the disturbances on the flow near the wing is small. However, there is some propagation of the disturbances downstream. Also, as shown in the figure, there is flow in the space between the main wing and SCF during contact, but it does not seem to be affecting the overall flow. An interesting aspect to point out is that after the SCF comes into contact with the main wing, it essentially cuts off flow across the leading edge of the main wing, resulting in flow separation off the slat/SCF. The separation creates two circulation regions and reattaches to the main wing downstream. This essentially combines the slat/SCF and main wing into one body. The effect diminishes near full slat retraction.

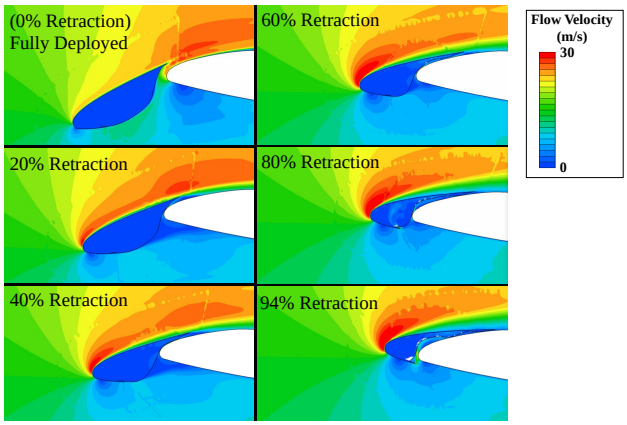

Figure 8. Velocity countours at various stages of slat retraction.

V. Wind Tunnel

Focus now shifts to the wind tunnel testing of the physical model. A description of the model is given followed by the implementation of the SCF. CFD and wind tunnel results are then compared.

[c]The SCF for the physical wind tunnel model had not been constructed at the time of the analysis.

A. Model Description

The scaled 2D section of the CRM wing is also used as the basis for the physical wind tunnel model. Figure 9(a) shows a Solidworks design of the model. The main structural support is an aluminum spar constructed out of a web and two plates (I-beam configuration). The outer mold line of the wing is obtained using 3D printed, plastic shells that are connected to the spar. Different slat/flap configurations are obtained using Firgelli L12 linear actuators that are housed inside the main-wing structure and are connected to the high-lift devices. The path for retraction/deployment of the high-lift devices is set by tracks cut into acrylic splitter plates positioned at both ends of the wing and a smaller steel plate at the midspan, inside the wing. Note that the steel guide plate splits the wing into two 0.61 m sections. Both the flaps and slats are 3D printed and stiffened using steel rods, which also served as pins for the retraction/deployment tracks. There are two versions of the slat: 1) the original slat from the CRM geometry and 2) a modified slat compatible with the SCF.

The model is connected to two ATI Delta F/T load cells, one on each side of the wing, in one of the Texas A&M University 3 ft-by-4 ft wind tunnel (see Fig. 9(b)) test sections. One of the load cells is free to rotate while the other is linked to a gear system that controls the angle of attack of the wing. The load cells have six degrees of freedom, meaning they can measure force and moment in three directions. However, for this work, only forces related to the lift and drag of the wing are of interest. Angle of attack is measured using a US Digital inclinometer and it is set to zero when the angle between the spar and floor is 0° (horizontal) as measured by a Lucas AngleStar digital protractor.[d]

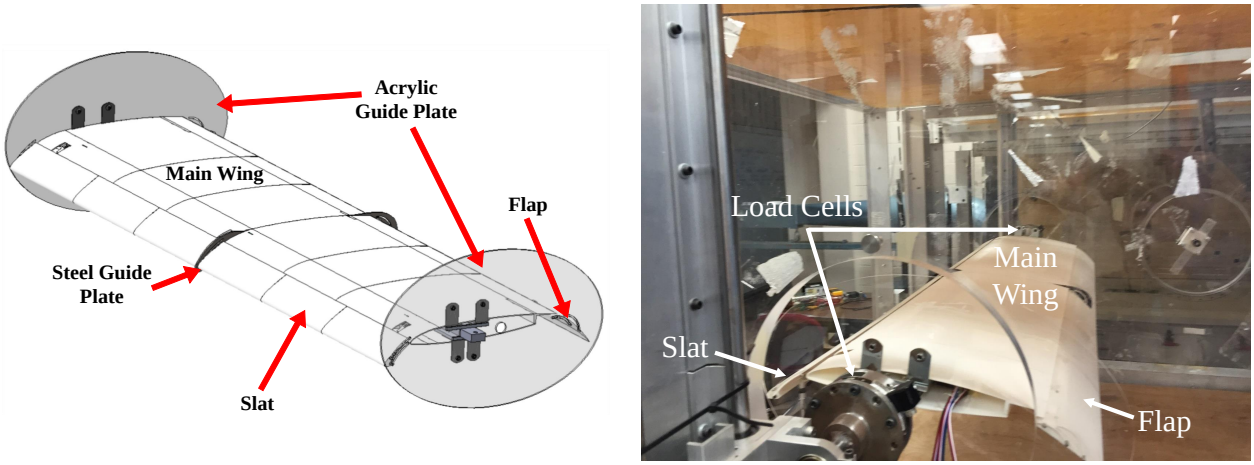

(a) Solidworks model.

(b) Physical model in test section.

Figure 9. Wind tunnel model of 2D section from CRM wing.

Pressure measurements on the surface of the main wing are enabled at quarter-span with a Pressure Systems Minature Electronic Pressure Scanner. Medical grade tubing connects drilled holes in the main wing surface to the pressure scanner. Wind-off (no flow) pressure measurements are used as the tare condition for the pressure measurements at wind-on conditions. Note that pressure is not measured on the slat and flap because neither high-lift device can accommodate the tubing due to their small solid sections.

B. SCF Implementation

At 6.25% scale, multi-flexure SCF designs are impractical for fabrication. Therefore, only a monolithic SCF design is considered in the current work. An SMA flexure with a thickness of 0.0762 mm (0.003 in) is chosen based on evaluations of various discrete flexure thicknesses that examined deflection and actuation force requirements for stowage. Based on design requirements, the zero stress state of the SMA SCF is its fully deployed profile. Therefore, shape setting through heat treatment is required since the purchased SMA material is a flat sheet. Creating a continuous SCF that spans the entire length of the wind tunnel model is not possible due to the size of the available furnace. Thus, smaller SCF sections are created. Shape setting

[d] An angle between the spar and floor of 0° corresponds to a model angle of attack of -1.48° (based on measurements in Solidworks).

of the SCF sections is conducted using a custom steel mold (see Fig. 10(a)), which is placed (with the SMA sheet inside) into a furnace at 600°C. The length of each mold is 7.62 cm (3 in). Longer SCF sections are created by linking multiple molds together in series. Note that shorter sections are treated for 22.5 min, while the longer SCF sections are treated for 30 min to account for the increased thermal mass due to the steel molds. After heat treatment, the molds containing the SCF are then water quenched.

Figure 10(b) shows the SCF attached to the slat. The slat has a steel trailing edge to improve the bonding of the SCF to the slat, paper hinges (bonded to slat-cove using epoxy) for the SCF to freely rotate and a steel cusp. The paper hinge axis is in the corner created by the slat-cove and steel cusp, and the length of the paper hinge connected to the SCF is approximately 8 mm. Note that conventional methods of connecting (bolts, screws, etc.) the slat and SCF are not feasible due to small size. Instead JB-Weld is used to bond the SCF to the trailing edge of the slat and the paper hinge.

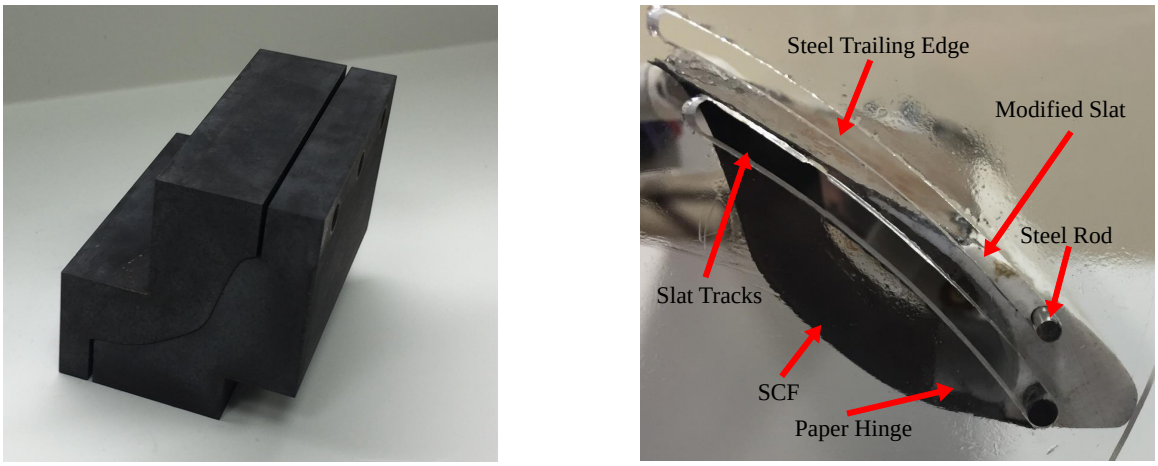

(a) Mold for shape setting SCF sections.

(b) Slat with SCF.

Figure 10. SCF implementation for CRM wind tunnel model.

C. Results and Comparisons

Wind tunnel testing of the CRM wing for both the retracted and deployed configurations is performed in the Texas A&M University 3 ft-by-4 ft tunnel at 15 m/s freestream velocity. Figure 11(a) shows the experimental and computational lift-AoA curves corresponding to the retracted configuration. At low angles of attack, both the measured and predicted data show a near-linear trend, but begin to flatten at higher angles. The lift from CFD results is generally higher at all angles compared to the experimental lift-AoA curve with the exception of the results corresponding to the CFD model at high angles under ≈laminar inlet flow. In addition, at higher angles of attack the discrepancy between the experimental and computational results increases. Some differences between the CFD and wind tunnel lift-AoA curves are expected since the wind tunnel model has geometric discontinuities (bolts, screws, actuators, etc.) that are not captured in the CFD model that represents a smooth, rigid body. In addition, the experimental results may be influenced by 3D flow effects introduced by the side walls and the steel guide plate. The fully developed turbulent flow case better matches experimental results as compared to the ≈laminar inlet flow case. Under ≈laminar inlet flow, the CFD lift-AoA curve flattens significantly while the other curves remain fairly linear. These results suggest that the inlet flow is not laminar.

Figure 11(b) shows the lift-AoA curves from experimental testing and CFD analysis for both deployed configurations. Similar to the CFD results in Section III, the experimental lift-AoA curves for the deployed and deployed-with-SCF configurations are similar, showing that there is not a significant impact on the lift due to the SCF. Both experimental and computational results show a nonlinear relation between the lift and angle of attack at low angles, which is followed by a near-linear trend. At low angles of attack (above -2°), the experimental lift-AoA curves better align with the curve from CFD analysis using ≈laminar inlet flow than the curve using fully developed turbulent flow. This is opposite of the results for the retracted configuration, which show that the fully developed inlet flow better matches the experimental results. To better model the turbulence and thus improve the CFD results, measurement of the test section turbulence

is needed. At high angles of attack, the experimental lift-AoA curves are lower in value than CFD results using both inlet flows. This difference between experimental and CFD results for the deployed configurations is due to the same factors (geometric discontinuities, surface roughness, side wall effects, etc.) that likely result in differences between the retracted lift-AoA curves. Also, at high angles of attack, there may be some fluttering/displacement of the slat and flap, which could lower the lift. The difference in lift may may also be due to blockage effects that can lower the freestream velocity.

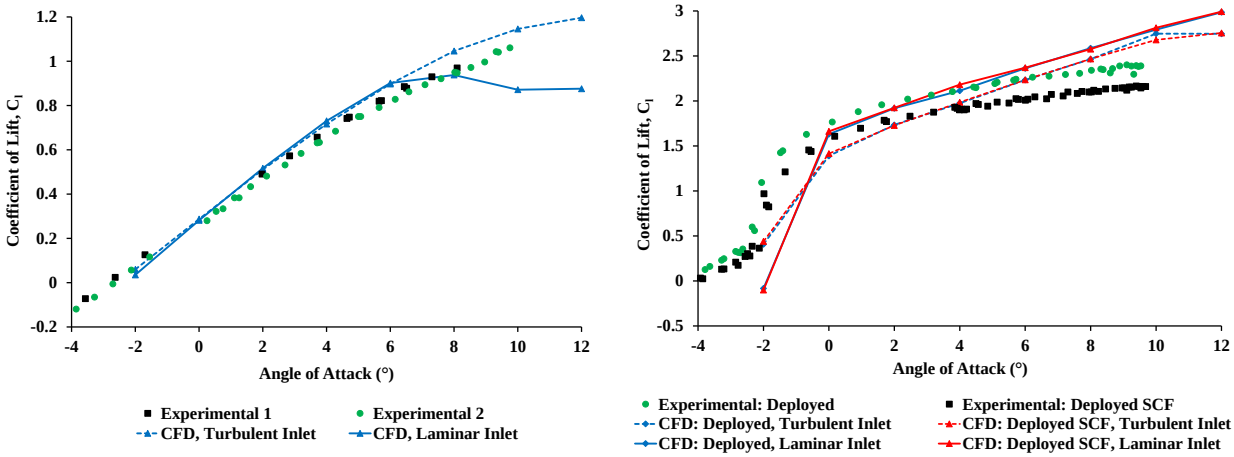

(a) Retracted. (b) Deployed.

Figure 11. Lift-AoA curves for both experimental and computational results.

The pressure along the main wing surface is measured at 4°, 6° and 8° angle of attack for the retracted and two deployed configurations. Figure 12 shows the coefficient of pressure distributions for the retracted configuration at 6° angle of attack from CFD analysis and wind tunnel testing. The CFD pressure distribution for both inlet flows matches well with the experimental distribution. This is not surprising due to the similarities between the lift-AoA curves. The distributions at 4° and 8° show a similar relation between the computational and experimental distributions.

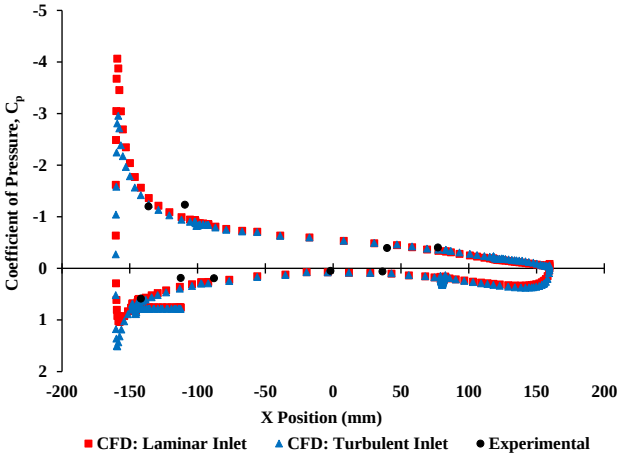

Figure 12. Coefficient of pressure distribution for retracted configuration at 6° angle of attack.

The coefficient of pressure distribution at 6° angle of attack from wind tunnel testing and CFD analysis for both deployed configurations is shown in Fig. 13. Similar to the retraction configuration results, the pressure distributions for the deployed configurations from wind tunnel testing are similar in overall shape and value to CFD results. The most noticeable difference between computational and experimental distributions is on the upper surface of the main wing near the leading edge. The pressure distribution from CFD analysis shows a lower suction peak compared to the experimental results. Also, though it is not shown, the difference between the distributions at the suction peak grows as the angle is increased. The pressure distributions along the surface of the main wing from CFD analysis for both deployed configurations are approximately the same, signaling that the pressure distribution along the main wing surface is not significantly affected by the SCF. However, wind tunnel testing shows the suction peak at the main wing leading edge is higher for the deployed-with-SCF configuration as compared to the deployed configuration. Note that apart from the leading edge, the distribution from experimental testing for both configurations is similar. CFD analysis using ≈laminar flow generally better matches the experimental distribution compared to the fully developed turbulence case since it calculates a higher suction peak.

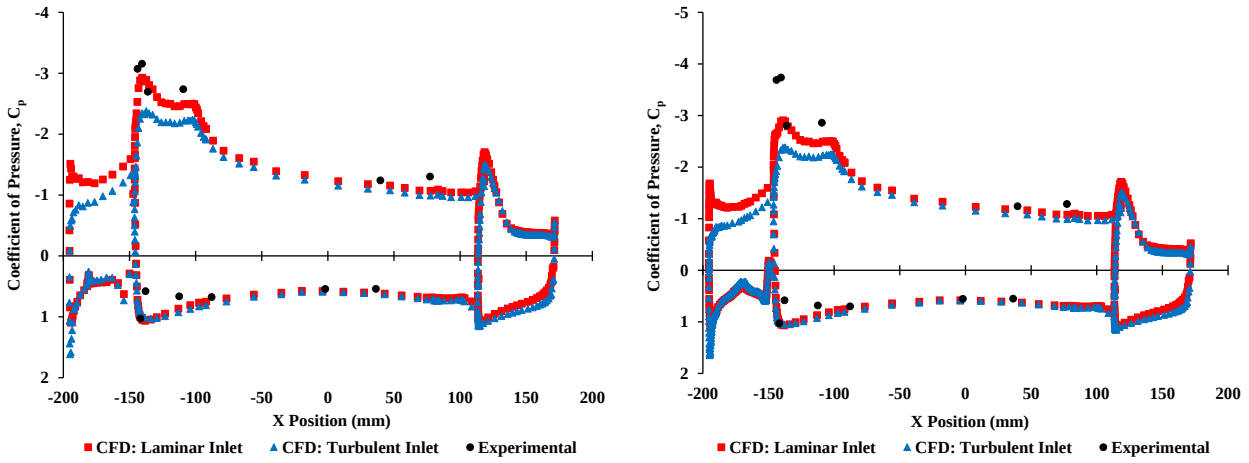

(a) Deployed.

(b) Deployed with SCF.

Figure 13. Coefficient of pressure distribution for both deployed configurations at 6° angle of attack.

VI. Summary and Conclusions

The goal of this work is to understand the behavior of the SMA SCF in flow using both computational tools and wind tunnel testing based on the CRM geometry. Specifically, this work focused on: 1) the development and analysis of CFD and FSI models for a scaled SCF configuration at multiple angles of attack and high lift device deployment levels and 2) development and testing of a wind tunnel model for validation of the computational results.

Prior to FSI analysis, CFD analysis of three CRM configurations was conducted to gain an initial understanding of how the SCF influenced the flow around the wing. Differences in the lift performance were observed between laminar and fully-turbulent freestream flow conditions. These differences were attributable primarily to differences in flow separation on the wing with the two freestream conditions. Also, the results showed that presence of the SCF did not significantly affect the lift performance of the wing.

Two load cases were considered for FSI analysis: 1) fixed, fully deployed and 2) slat retraction. The analysis for the fixed, fully deployed case was conducted at angles of attack of 6° and 8° with 15 m/s inlet velocity. The maximum SCF displacement for both angles was approximately 0.03 mm, which was similar to results from static analysis. Fluctuation of the displacement (vibration) had a small amplitude and frequency characteristics that were similar to the predicted lift performance. Additional work is required to determine if this effect is numerical noise or if it has a physical counterpart. FSI analysis of the slat retraction was largely successful, but zero volume elements resulted in an analysis crash at 94% retraction. This was believed to be one of the first FSI analyses of an SMA morphing structure undergoing significant changes in volume due to rigid-body kinematics and contact.

A wind tunnel model of a scaled 2D section of the CRM wing was built and tested in order to validate computational results. This was the first wind tunnel testing of a flexible SCF. Comparisons of the experimental and computational lift-AoA curves showed similar trends for all considered configurations. Comparisons of the coefficient of pressure distribution showed that experimental and CFD results matched well with the exception of the suction peak at the main wing leading edge.

Future work will focus on continued development of the fluid models. Overall accuracy of the analysis will be improved by removing the local disturbance propagation caused by the overset meshes. Also, turbulence measurements of the tunnel will improve the modeling of the flow at the inlet. Thinner SMA flexures may be considered in order to observe larger aeroelastic responses from both the physical and computational models. Finally, future work will develop nonlinear reduced order models of the SCF under flow for the purpose of design studies and optimizations. Due to computational runtimes, the current FSI implementation is not feasible for any design study.

References

[1] Gleine, W., Mau, K., and Carl, U., "Aerodynamic Noise Reducing Structure for Aircraft Wing Slats," US Patent Nol US 6,394,396 B2, May 28,2002.

[2] Streett, C., Casper, J., Lockard, D., Khorrami, M., Stoker, R., Elkoby, R., Wenneman, W., and Underbrink, J., "Aerodynamic Noise Reduction for High-Lift Devices on a Swept Wing Model," AIAA Paper 2006-212, 2006.

[3] Horne, W., James, K., Arledge, T., Soderman, P., Burnside, N., and Jaeger, S., "Measurements of 26percent-scale 777 Airframe Noise in the NASA Ames 40 by 80 Foot Wind Tunnel," AIAA Paper 2005-2810, 2005.

[4] Imamura, T., Ura, H., Yokokawa, Y., Enomoto, S., Yamamoto, K., and Hirai, T., "Designing of Slat Cove Filler as a Noise Reduction Device for Leading-edge Slat," AIAA Paper 2007-3473, 2007.

[5] Turner, T., Kidd, R., Hartl, D., and Scholten, W., "Development of a SMA-based Slat-Cove Filler for Reduction of Aeroacoustic Noise Associated with Transport-Class Aircraft Wings," *Proceedings of the SMAE 2013 Conference on Smart Materials, Adaptive Structures, and Intelligent Systems*, SMASIS2013-3100, ASME, 2013.

[6] Scholten, W., Turner, T., and Hartl, D., "Analysis-Driven Design Optimization of a SMA-Based Slat-Cove Filler for Aeroacoustic Noise Reduction," *Proceedings of the ASME 2013 Conference on Smart Materials, Adaptive Structures, and Intelligent Systems*, SMASIS2013-3104, ASME, 2013.

[7] Scholten, W., Hartl, D., Turner, T., and Kidd, R., "Development and Analysis-Driven Optimization of a Superelastic Slat-Cove Filler for Airframe Noise Reduction," *AIAA Journal*, Vol. 54, No. 3, 2016, pp. 1078-1094.

[8] Chin, V., Peters, D., Spaid, F. and McGhee, R., "Measurements about a Multi-element Airfoil at High Reynolds Numbers," AIAA Paper 1993-3137, 1993.

[9] Scholten, W., Hartl, D., Strganac, T., Turner, T., "Reduction of Actuation Loads in a Self-Deploying SMA-Based Slat-Cove Filler for a Transport Aircraft," *Proceedings of the ASME 2015 Conference on Smart Materials, Adaptive Structures, and Intelligent Systems*, SMASIS2015-9015, ASME, 2015.

[10] Scholten, W., Patterson, R., Volpi, J., Chapelon, Q., Hartl, D., Strganac, T., and Turner, T., "Noise Reduction in a High Lift Wing Using SMAs: Computational Fluid-Structural Analysis," *Proceedings of the ASME 2016 Conference on Smart Materials, Adaptive Structures, and Intelligent Systems*, SMASIS2016-9196, ASME, 2016.

[11] Lacy, D., and Sclafani, A., "Development of the High Lift Common Research Model (HL-CRM): A Representative High Lift Configuration for Transonic Transports,", AIAA Paper 2016-0308, 2016.

[12] SC/Tetra, *User's Guide*, Software Cradle Co., Ltd., 2015.

[13] Menter, F., "Zonal Two Equation k-ω Turbulence Models for Aerodynamic Flows,", AIAA Paper 1993-2906, 1993.

[14] Abaqus, *Analysis User's Manual*, Dassault Systemes of America Corp., Woodlands Hills, CA, 2011.

[15] Lagoudas, D., Bo, Z., and Qidwai, M., "A unified thermodynamic constitutive model for SMA and finite element analysis of active metal matrix composites,", Mechanics of Composite Materials and Structures, 1996.

[16] ASTM International, "Standard Test Methods of Tension Testing of Metallic Foil," 2016.